Momentum Transfer Resolved Electron Correlation Microscopy

Shuoyuan Huang, Paul M Voyles*

Department of Materials Science and Engineering, University of Wisconsin Madison, Madison, Wisconsin 53706, USA * paul.voyles@wisc.edu

Abstract Electron correlation microscopy (ECM) characterizes local structural relaxation dynamics in fluctuating systems like supercooled liquids with nanometer spatial resolution. We have developed a new type of ECM technique that provides moderate resolution in momentum transfer or k space using five-dimensional scanning transmission electron microscopy. k-resolved ECM on a Pt_{57.5}Cu_{14.7}Ni_{5.2}P_{22.5} metallic supercooled liquids measures rich spatial and momentum structure in the relaxation time data $\tau(r, k)$. Relaxation time maps $\tau(r)$ at each azimuthal k are independent samples of the material's underlying relaxation time distribution, and τ of radial k shows more complex behavior than the de Gennes narrowing observed in analogous X-ray experiments. We have determined the requirements for electron counts per k-pixel, number of k-pixels per speckle, and time sampling to obtain reliable k-resolved ECM data.

Keywords: 5D STEM; electron correlation microscopy; supercooled liquids dynamics; *k*-dependent dynamics

1. Introduction

Electron correlation microscopy (ECM) studies local relaxation dynamics in supercooled liquids (SCLs) and potentially other fluctuation systems using time-resolved coherent electron nanodiffraction [1,2]. Speckle patterns created by coherent electron scattering encode the structure of small volumes of atoms in the sample. The fluctuation of speckle intensity in time arises from changes in structure and can be used to analyze the structural relaxation dynamics. ECM experiments have been carried out primarily in a tilted dark field (TDF) transmission electron microscopy (TEM) configuration. The spatially resolved parallel illumination of TDF type ECM enables characterization of localized dynamics at nanometer scale [3]. Using this configuration, ECM was used in studying the fast surface dynamics of metallic SCLs [4] and phasecomposition dependent dynamics [5]. A major drawback of TDF type ECM is its lack of momentumtransfer- or k-resolution: TDF TEM experiment collects and integrates the diffracted intensity from a single k region defined by the objective aperture, typically placed at the first diffraction ring of the sample. This geometry means the relaxation time measurement depends on only one k (or an average of k's that fit through the aperture), which represent only a subset of the entire system's dynamics. Nakazawa and Mitshuishi recently implement ECM using in situ four-dimensional scanning transmission electron microscopy (4D STEM) [6], but a relatively slow camera and data analysis that started by reconstructing virtual aperture TDF images meant no increase in *k* resolution.

Relaxation dynamics in SCLs are spatially heterogeneous [7–9], meaning that the SCL is comprised of a distribution of nano-sized dynamic domains, each of which has different characteristic relaxation time. Each of those domains has the potential to diffract at different k, given potential differences in orientation and internal structure. By confining accessible dynamics to only one k defined by the objective aperture, TDF type ECM limits the number of dynamic domains studied and might lead to incomplete dynamic distribution due to the lack of sampling. Careful examination of the dynamic heterogeneity from a complete distribution is of great importance to study the relaxation behavior and glass transition [10–12]. Relaxation dynamics in SCLs also show different k-dependencies in different dynamics regimes under different

temperatures [13] or atomistic or molecular details [14,15]. *k*-resolved dynamics in metallic SCLs and network glasses have been studied using X-ray photon correlation spectroscopy (XPCS) [16,17], showing the importance of studying *k*-dependent dynamics in understanding the complex relaxation mechanisms. For multicomponent glass, *k*-dependent dynamics can indicate structural- and compositional dependency in relaxation dynamics.

Here, we develop the experiment and analysis protocol for five-dimensional scanning transmission electron microscopy (5D STEM) type ECM that captures both real space- and *k*-resolved relaxation dynamics and apply this method to Pt_{57.5}Cu_{14.7}Ni_{5.2}P_{22.5} metallic SCL. Experimental requirements for electron counts, the number of *k* pixels that sample each speckle, and the time sampling are described. We find that a set of relaxation time measurements computed from speckles at the same *k* magnitude but at different azimuthal angles show different values and spatial domain patterns, but they have the same mean and log-normal statistical distribution. These results confirm that different domains in the SCL diffract in different directions and demonstrate that an abundance of information can be obtained from a single 5D STEM acquisition. Potential applications utilizing the 5D STEM ECM are discussed, including studying momentum-transfer-dependent and time-dependent dynamic processes.

2. Methods

2.1 Sample preparation

Pt_{57.5}Cu_{14.7}Ni_{5.2}P_{22.5} metallic glass nanowires were synthesized using nanomoulding method as described in [18]. The as-fabricated nanowires were attached to a substrate plate of the bulk metallic glass with the same composition. The plate was first rinsed with deionized water and isopropyl alcohol. Then the plate was immersed in methanol and sonicated for 15 min to release the nanowires. The nanowire dispersion in methanol was dropped onto a DENSSolutions Wildfire TEM heating chip using a micropipette. We dropped 1.5-1.8 μ L at a time for 10-12 drops with 5 min interval to allow methanol evaporation. The TEM sample was plasma-cleaned in 20 psi Ar + O₂ for 10 min to remove organic residues. We then deposited 10 nm thick amorphous carbon layer to prohibit fast surface dynamics [4].

2.2 5D-STEM experiments and data analysis

The 5D STEM experiments are performed on a 200 kV FEI Titan G2 microscope operated in micro-probe STEM mode. A probe convergence angle of 1.53 mrad was used, generating a probe size of 1 nm. Spot size 5 was chosen for the experiments to obtain a relatively high probe current of 25 pA while maintaining enough partial coherence [19,20]. The sample is heated to the designated temperature via a DENS Wildfire heating holder. Nanodiffraction patterns were acquired using an ultrafast DE-Celeritas camera [21] at 256 by 128 readout area. The scan controller system for 4D and 5D STEM acquisition is described in [22].

Figure 1 is a schematic of 5D STEM acquisition and ECM analysis. A coherent probe is scanned across the region of interest in a 2D grid and a 2D diffraction pattern is collected at each scan position. The 4D STEM scan is repeated without interruption. This creates a five-dimensional dataset I(r, k, t), where r = (x, y) is the real space coordinate, $k = (k_x, k_y)$ is the reciprocal space coordinate, and t is time. To correct for sample drift, the collected 5D dataset is registered along the real space axes using cross-correlation applied to a virtual dark field image time series computed from the 5D data. Since the diffraction frames are sparse in electrons and too low in intensity to be useful outside the first diffraction ring, the dataset is then polar transformed in reciprocal space axes into $I(r, k_p, t)$, where $k_p = (k_r, k_\phi)$, k_r is the radial component and k_ϕ is azimuthal component. Only a strip of the polar transformed pattern covering k_r from 0.3 Å⁻¹ to 0.6 Å⁻¹ corresponding to the first peak in diffraction intensity is used for further analysis.

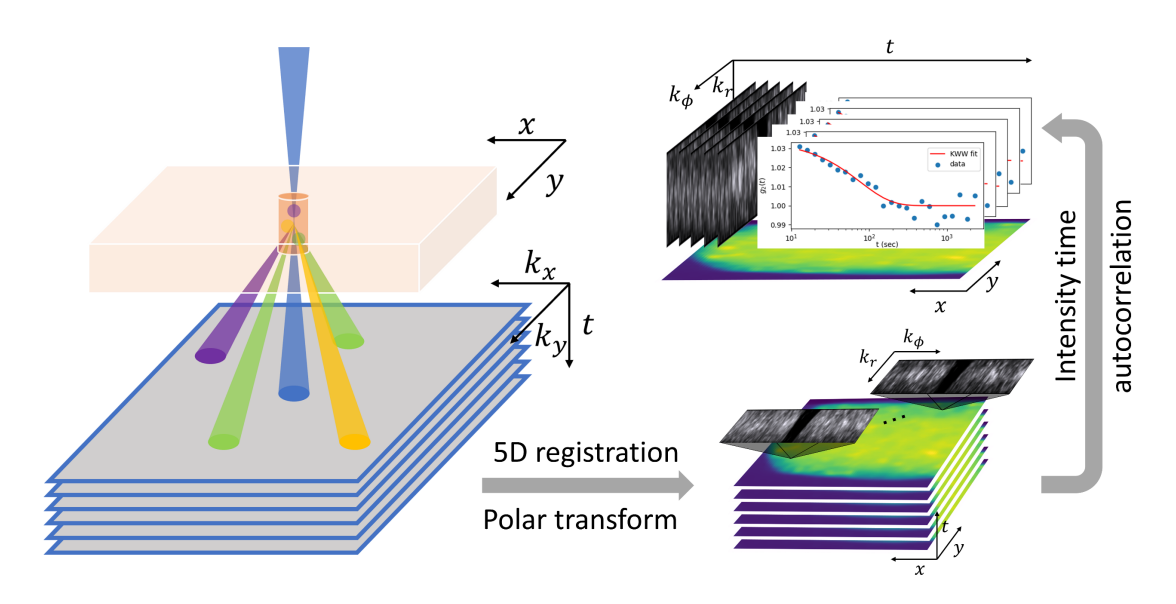


Figure 1. Schematics of 5D STEM acquisition and *k*-resolved ECM analysis. Repeated cycles of 4D STEM acquisition create a 5D dataset. Raw data are preprocessed and compressed before being registered along the real space axes and polar transformed across the reciprocal axes. The intensity time correlation functions are calculated for each real and polar reciprocal pixel to extract relaxation times.

To access the relaxation dynamics represented by the intensity fluctuations, time autocorrelation function of the diffracted intensities at each (r, k_p) pixel is calculated using

$$g_2(\mathbf{r}, \mathbf{k}_p, t) = \frac{\langle I(\mathbf{r}, \mathbf{k}_p, t') I(\mathbf{r}, \mathbf{k}_p, t + t') \rangle_{t'}}{\langle I(\mathbf{r}, \mathbf{k}_p, t') \rangle_{t'}^2}.$$
 (1)

The time correlation function of the coherent diffraction intensity is fit to Kohlrausch-Williams-Watt (KWW) function [23]

$$g_2(t) = 1 + A \exp\left[-2\left(\frac{t}{\tau}\right)^{\beta}\right],\tag{2}$$

where τ is relaxation time, β is the shape parameter related to dynamic heterogeneity [9], and A is an instrument-dependent parameter related to probe coherence [24] and other factors. By fitting experimentally obtained $g_2(r, k_p, t)$ to the KWW function for each (r, k_p) pixel, we obtain real and reciprocal space resolved relaxation times $\tau(r, k_p)$.

The raw experimental data can have size from several hundred GB to a few TB. The raw data were preprocessed by dark and gain correction and setting pixels below a threshold value of 7 digital counts to zero. Then it is stored in a compressed format optimized for subsequent analysis [25]. The whole analysis procedure is parallelized on a high-performance computing cluster using the HpyerSpy [26] and pyXem [27] python packages.

3. Results and Discussion

3.1 Interpretation of relaxation times versus r and k

ECM analysis from 5D STEM experimental data generates a data hypercube of relaxation times, $\tau(r, k_p)$, which contains a rich amount of information. At fixed k_p , $\tau(r)$ represents the spatial distribution of the

projection of dynamic domains that contains structures that diffract at k_p . This is illustrated in Fig. 2, where the dynamic domains marked red diffract to the same $k_p = k_1$, and $\tau(r, k_p = k_1)$ maps the spatial distribution of that particular subset of dynamic domains. This geometry is analogous to TDF type ECM where the objective aperture is placed at k_p . One 5D-STEM experiment can obtain a large amount of relaxation time measurements equivalent to tens or hundreds of TDF experiments. On the other hand, at fixed r, $\tau(k_p)$ can be treated as a distribution of dynamic domains inside the probed volume at r but separated in depth along the column of the sample illuminated by the probe. This is illustrated in the first column in Fig. 2, where domains marked with different colors at various depths diffracts at different k_p . Due to the diffraction geometry, $\tau(k_p)$ lose all the spatial information regarding the position of the domains inside the thickness.

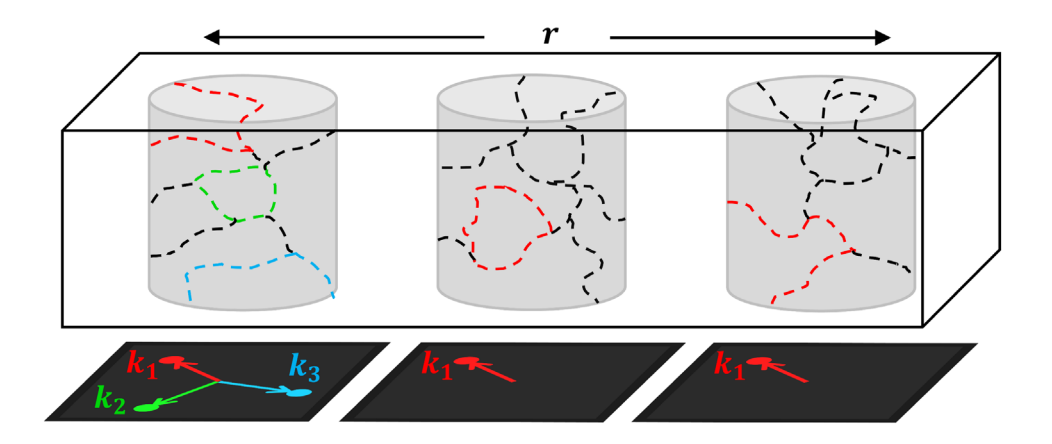


Figure 2. Illustration of correspondence between relaxation measured at different r and k and different dynamic domain distributions in the sample.

Figure 3a shows relaxation time maps of a $Pt_{57.5}Cu_{14.7}Ni_{5.2}P_{22.5}$ nanowire heated to 511 K (T_g+4 K) reconstructed at different azimuthal k_{ϕ} but at the same radial $k_r=0.46$ Å⁻¹. These maps are spatial representation of dynamic domains with structures that have similar interatomic distances but different orientations causing diffraction in different directions. They show heterogeneous domains with different characteristic times. While the overall relaxation time scale and length scale are similar, their microscopic details are different. Fig 3b shows that at a fixed spatial position, relaxation time varies with k_{ϕ} . However, all of these data are drawn from the same underlying distribution of relaxation behavior. Fig. 3c shows the histograms of $\tau(r)$ at different k_{ϕ} . They exhibit the same log-normal distribution, with the same median as ensemble relaxation time, indicating they are taken from the same dynamic ensemble [28]. This suggests the relaxation time maps $\tau(r)$ like the ones in Fig. 3a are independent samples of the dynamics of this nanowire, each of which is descriptive to the dynamics of the whole system at the corresponding k_r . We will use the median relaxation time calculated at each k_{ϕ} then averaged over all k_{ϕ} to represent the ensemble average relaxation time for the remainder of this paper. The dynamic dependency on k_r will be discussed in a following section.

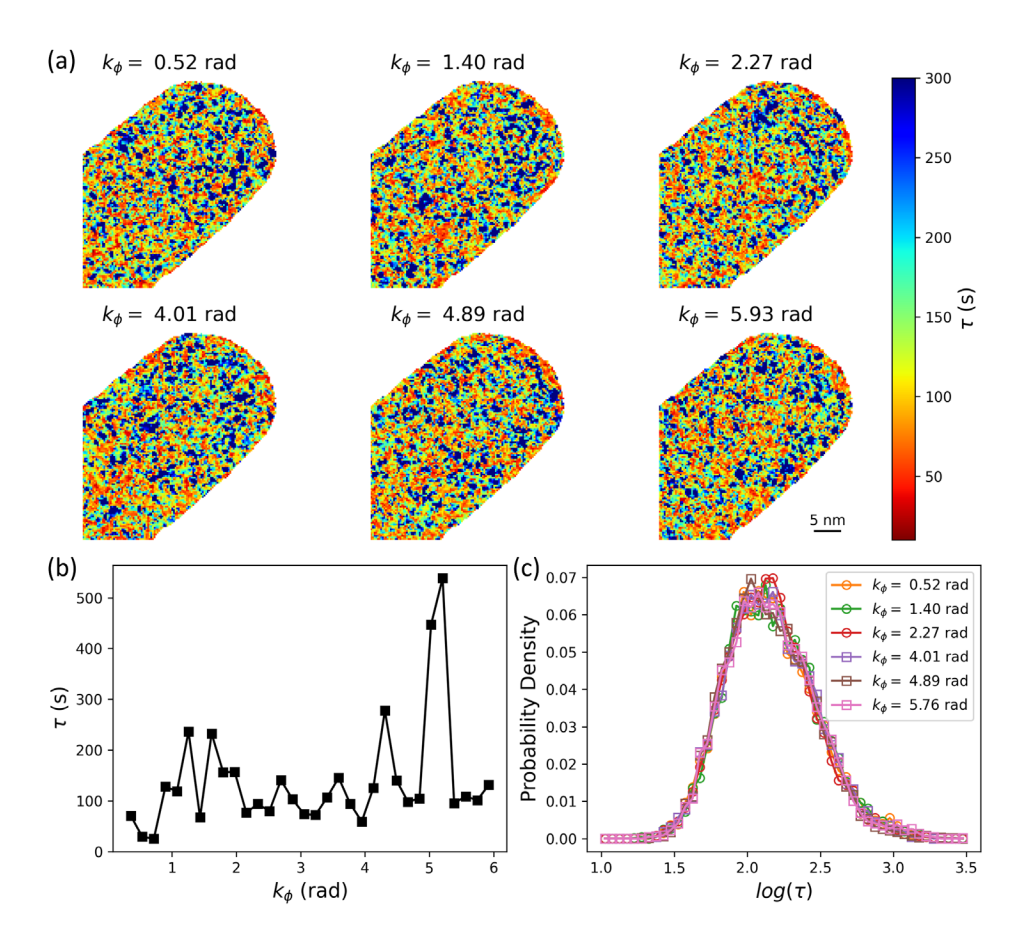


Figure 3. (a) Relaxation time maps of Pt_{57.5}Cu_{14.7}Ni_{5.2}P_{22.5} nanowire at 511 K from $k_{\phi} = 0.52$, 1.40, 2.27, 4.01, 4.89, and 5.93 rad with a fixed $k_r = 0.46$ Å⁻¹; (b) Measured relaxation times versus k_{ϕ} at a fixed real space position and k_r ; (c) Histograms of relaxation times maps $\tau(r)$ from different k_{ϕ} at the same k_r .

3.2 Effects of electron counts and time-sampling

k-resolved ECM experiments push the capabilities of detectors, sources, and data handling, so obtaining reliable quantitative results requires careful consideration of the influence of experimental design on the quality and accuracy of the time autocorrelation function $g_2(t)$. The major source of experimental uncertainty in relaxation time measurement comes from noise in g_2 . The signal-to-noise ratio (SNR) of g_2 from a coherent scattering intensity time series is given by [29]

$$SNR = A \cdot I_e \cdot N \cdot t \cdot \sqrt{N_s},\tag{3}$$

where A is the instrument-dependent parameter from Eq. (2), I_e is the electron count rate in electrons per pixel per second, N is the number of detector pixels used to calculate g_2 , t is the exposure time of each frame (the inverse of detector frame rate), and N_s is the number of time samples, which is also the number of 4D STEM scan cycles. To increase the SNR, one can simply perform longer experiments. However, acquiring long experiments can be infeasible due to limitations imposed by sample drift and data size [5]. In addition, if the total duration becomes comparable to the persistence time of the dynamic domains, one g_2 measurement would no longer be characteristic for a single relaxation time of one dynamic domain as described by Eq. (2) [30]. The electron count rate is controlled by both detector frame rate and probe current,

but probe current cannot be increased without sacrificing probe coherence [19]. This leaves decreasing frame rate as the remaining way to increase the g_2 SNR.

Figure 4a compares g_2 calculated from data acquired using 3600 fps and 19600 fps detector frame rate with all other parameters the same for a Pt_{57.5}Cu_{14.7}Ni_{5.2}P_{22.5} nanowire at 519 K. Unlike the high count g_2 , the low count g_2 displays higher noise level and barely shows a decay with time. Fig. 4b shows the average relaxation time at 519 K measured from datasets with different frame rates plotted against the electron counts per pixel in the first diffraction ring. The detector frame rates were 3600, 4900, 6400, 10000, 19600, and 40000 fps, and the scanning size and field of view is changed for each frame rate to keep a constant time sampling rate of 0.25 seconds per 4D scan. At low electron counts, the measured average relaxation time becomes very small value due to large g_2 SNR. For electron counts above ~ 1 electron per pixel, the average relaxation time plateaus to a constant value that can be viewed as the high electron count limit. These results show that an electron count of at least 1 per pixel at the first diffraction ring should be used for k-resolved ECM experiments.

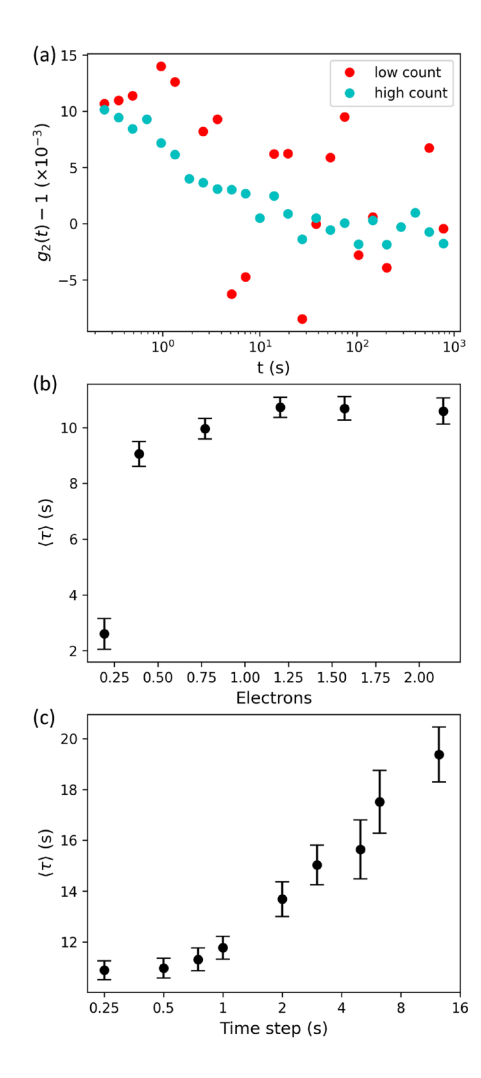


Figure 4. (a) Example time autocorrelation functions g_2 calculated from datasets with low and high electron counts; (b) Measured average relaxation times versus electron counts with fixed time sampling; (c) Measured average relaxation times versus time step with fixed electron counts as a function of time sampling. Error bars in (b) and (c) are standard deviations of many different azimuthal k.

Changing frame rate influences the time sampling of the experiments as well as the electron counts. In TDF ECM, a minimum time sampling rate of 0.1 τ was found to be required [2]. As the time step between each frame grows larger, sampling of the relaxation events eventually becomes inadequate. Fig. 4c shows the effect of time sampling rate for 5D-STEM type ECM. The time step is adjusted during analysis, while the electron count is fixed by using a single experimental dataset collected at the frame rate of 3600 fps. The measured average relaxation time diverges once the time step between each 4D scan becomes larger than 1/20 relaxation time, twice the requirement of TDF-ECM. This may reflect lower counts in the 5D STEM experiment, but it may also arise because the 5D STEM intensity time series at one position is not continuous. These results suggest that, on average, each relaxation event should be sampled at least 20 times to obtain a reliable measurement.

The following inequalities summarize the constraints on the acquisition parameters for a reliable, quantitative 5D-STEM experiment for k-resolved ECM:

$$\frac{N_x N_y}{f} < 0.05\tau,\tag{4}$$

$$\frac{l_s}{fN_d} > 1. ag{5}$$

 N_x , N_y are scanning size in each scan direction, f is the detector frame rate, I_s is the diffracted electron current (in electron per second) which depends on the probe current, sample composition and thickness, and N_d is the number of detector pixel in the first diffraction ring. τ is the ensemble average relaxation time to be measured, which must be known, or at least estimated from, for example, viscosity data. Eq. 4 represents the time sampling requirement and Eq. 5 represents the electron counts requirement. In practice, it might be unfeasible to satisfy these two requirements while maintaining enough spatial sampling, in which case a time sampling rate of 0.1τ can be used instead. As shown in Fig. 4c, less than 10% of deviation in relaxation time measurement is observed between time steps of 0.05τ and 0.1τ .

3.3 Azimuthal k sampling

Next we consider how many pixels are needed in a 5D STEM diffraction pattern for ECM. Can ECM be performed with small format detectors? What are the limits on reducing detector pixels to increase readout or binning pixels pre- or post-acquisition to increase electrons counts? In general, it is preferable to bin the polar transformed data $\tau(r, k_p)$ in the azimuthal k_{ϕ} direction, rather than radial k_r , because an isotropic SCL will have no preferred k_{ϕ} , but different k_r may correspond to scattering by different interatomic spacings. Fig. 5a demonstrates the value of increased signal from k_{ϕ} binning by comparing g_2 calculated from data with no binning and from data binned by 8 in k_{ϕ} . g_2 from binned data shows improved SNR without changing the shape of g_2 .

However, it is possible to use pixels that are too large compared to the size of the speckles, which is set by the probe convergence angle. Fig. 5b shows the measured average relaxation time versus $\Delta k_{\phi}/k_{c}$, the ratio between the pixel size Δk_{ϕ} and probe convergence angle k_{c} , where Δk_{ϕ} has been adjusted by post-acquisition binning of originally finely-sampled data. At small pixel size, increasing Δk_{ϕ} increases SNR, resulting in more accurate relaxation time measurement. This effect is more pronounced for data with lower electron counts, as seen by comparing 19600 fps and 10000 fps data. However, as the pixel size increases, the measured relaxation time does not converge but instead keeps increasing. Once the bin size becomes larger than the convergence angle or the speckle size, i.e. $\Delta k_{\phi}/k_{c} > 1$, fluctuations of intensity from nearby diffraction speckles are summed in a single measurement, which appears to result in g_{2} that are more

strongly influenced by events with longer τ , making measured average relaxation time artificially larger. Fig. 5c shows this effect in binned diffraction patterns. For $\Delta k_{\phi}/k_{c} < 1$, the binned data show higher SNR with little to no loss in speckle features, but for $\Delta k_{\phi}/k_{c} > 1$, neighboring diffraction features are merged causing loss of information. Therefore, $k_{\phi} \leq k_{c}$ is optimal for increasing SNR without reducing sensitivity to diffraction intensity fluctuation.

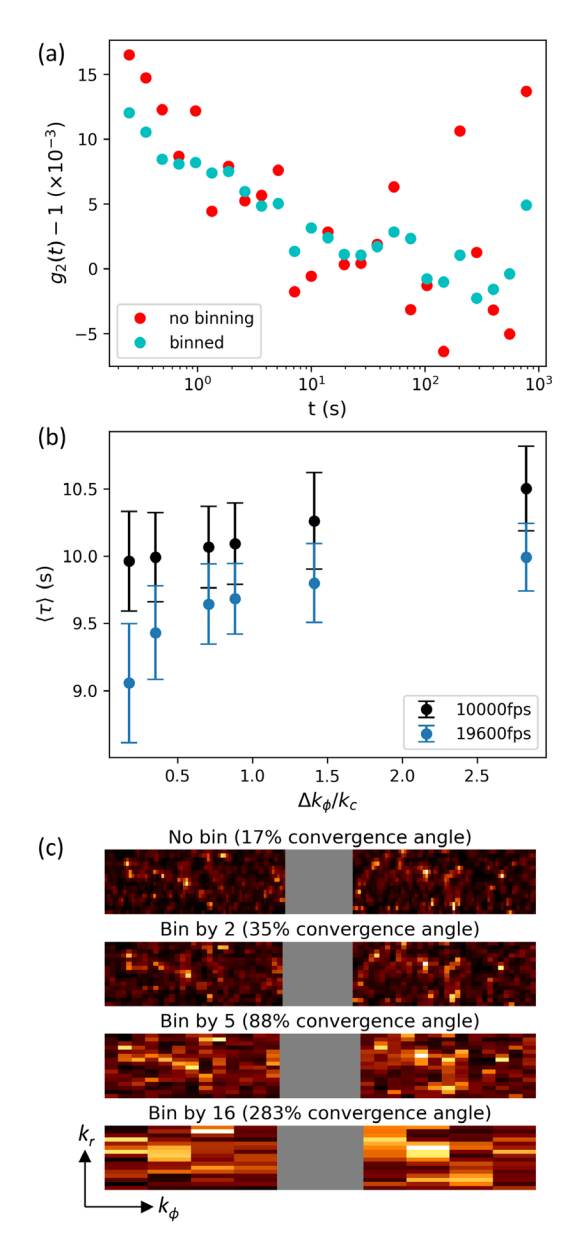


Figure 5. (a) Example time autocorrelation functions g_2 calculated from dataset with no binning and a binning factor of 8 in azimuthal k direction; (b) Measured average relaxation times versus the ratio of k_{ϕ} bin size to convergence angle for 10000 and 19600 fps data. Error bars are standard deviations of many different azimuthal k; (c) An example polar transformed diffraction pattern at 4 different k_{ϕ} . k_{ϕ} and k_r axes are not to on the same scale.

3.4 Application of k-resolved ECM

A major advantage of k-resolution from 5D-STEM type ECM experiments is the ability to study momentum-transfer-dependent dynamics. Fig. 6a shows the ensemble average relaxation time versus k_r for $Pt_{57.5}Cu_{14.7}Ni_{5.2}P_{22.5}$ SCL measured at 511 K. Data acquired in this k range all have intensities above 1 electron count per pixel, therefore the measured relaxation time is independent of electron counts according to Fig. 4b. The relaxation time shows a peak shape profile with peak around the first diffraction peak of electron diffraction. This behavior is similar to de Gennes narrowing observed in various glassy systems [15,31]. However, it does not coincide exactly with the diffraction peak, suggesting a more complex mechanism perhaps due to composition/structure dependent dynamics. A similar attempt in studying structure-dynamic relationships has been made recently using virtual reconstruction of *in situ* 4D STEM acquisitions and correlatively comparison with diffraction intensity variance [32].

The relaxation mechanism studied by k-dependent dynamic using XPCS and neuron scattering utilizes a larger k-range than just the first diffraction peak [17,33,34]. While 5D STEM type ECM can only characterize relaxation time in a narrower k-range (the first diffraction peak) due to the weak signal outside that range, it provides microscopic spatial information of the relaxation dynamics. Connecting the length scale and time scale of the relaxation dynamic is critical to understanding the slowdown of dynamic during glass transition [35]. Fig. 6b shows the average relaxation domain size ξ_{τ} versus relaxation time at 511 K. The domain size ξ_{τ} is measured by calculating the spatial autocorrelation function of the relaxation time maps $\tau(r)$ and fitting it to a 2D Gaussian function. The FWHM of the Gaussian function is used as ξ_{τ} . We can see ξ_{τ} vs. τ at this one temperature appears to have two branches of scaling corresponding to the lower k and higher k legs of the diffraction intensity peak, respectively. They both exhibit power law dependences consistent with conventional dynamic scaling [36–38]. This bifurcation of $\xi_{\tau}(t)$ scaling is potentially due to differences in compositional and structural detail between low and high k, although the range of time scales and length scales studied here is too small to draw strong conclusions.

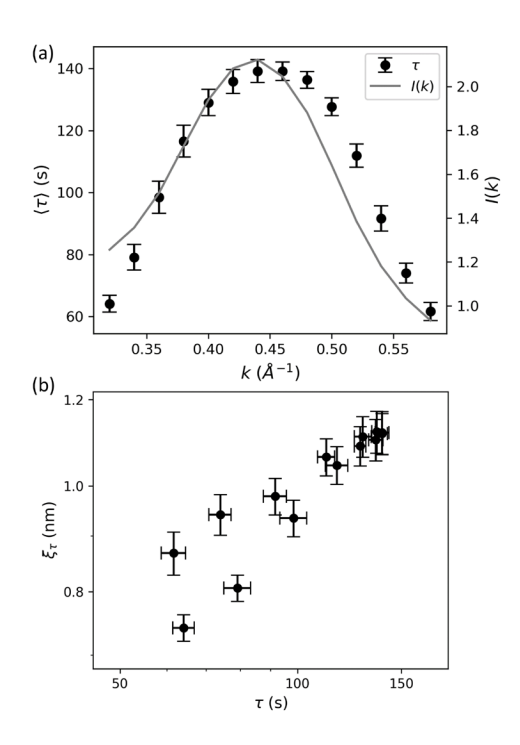


Figure 6. (a) Measured average relaxation time versus k_r for Pt_{57.5}Cu_{14.7}Ni_{5.2}P_{22.5} SCL at 511 K. Gray line is diffraction intensity profile I(k); (b) Log-log plot of dynamic length scale represented by dynamic

domain size ξ_{τ} versus average relaxation time at each k_r . Error bars are standard deviations of many different azimuthal k.

The multi-dimensionality of 5D STEM also enables calculation of higher order correlation functions, such as two-time correlation function (TTCF). TTCF can be used to characterize non-equilibrium and therefore time dependent dynamic processes such as aging and rejuvenation [39–41]. TTCF is calculated from 5D dataset by

$$G(t_1, t_2) = \frac{\langle I(t_1)I(t_2)\rangle_k}{\langle I(t_1)\rangle_k \langle I(t_2)\rangle_k},\tag{5}$$

where t_1 , t_2 are two times, and the $\langle ... \rangle_k$ average is performed over all k pixels in the first diffraction ring. Fig. 7a shows TTCF at one spatial position for $Pt_{57.5}Cu_{14.7}Ni_{5.2}P_{22.5}$ measured at 511 K. The bright spots on the diagonal line $t_1 = t_2$ represent individual relaxation events inside the probed volume at this scan position. Fig. 7b shows positional averaged TTCF for the entire nanowire. The width of the diagonal band marked by the white lines is proportional to the average relaxation time at each time elapse during the acquisition[42]. The width fluctuates slightly, suggesting the sample was in (metastable) equilibrium during the experiment, although the slight widening at the end might indicate intermittent physical aging [43] or perhaps the onset of fluctuations leading to crystallization.

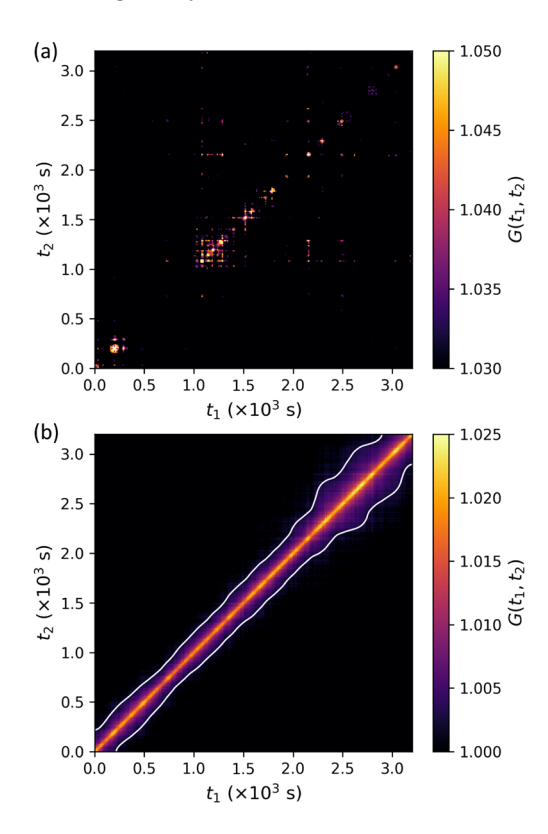


Figure 7. (a) TTCF at one spatial position for $Pt_{57.5}Cu_{14.7}Ni_{5.2}P_{22.5}$ SCL measured at 511 K; (b) Spatial averaged TTCF for a $Pt_{57.5}Cu_{14.7}Ni_{5.2}P_{22.5}$ nanowire sample at 511 K. White lines are contours when $G(t_1, t_2) - 1$ decays to $1/e^2$ of $G(t_1 = t_2)$.

4. Conclusion

We performed momentum-transfer-resolved ECM using 5D STEM acquisition on glassy $Pt_{57.5}Cu_{14.7}Ni_{5.2}P_{22.5}$ nanowires heated above glass transition temperature. Reconstruction of relaxation time data hypercube $\tau(r, k)$ provides dynamic information resolved in both real- and momentum-transfer-space. The experimental condition required for a reliable measurement of average relaxation time is determined. A guideline described by two inequalities is provided for experimental design of 5D STEM type ECM. The experimental parameters are limited by the electron count, which should preferably be higher than one electron per pixel at the first diffraction ring, and the time sampling, which needs to be faster than one 4D scan every 0.1τ . Post-acquisition binning of data in k_{ϕ} direction is needed if the electron counts is low in raw data. A bin size around the speckle size or the probe convergence angle is ideal. From momentum-transfer-resolved ECM experiment on $Pt_{57.5}Cu_{14.7}Ni_{5.2}P_{22.5}$ SCL at 511 K, we find that each k_{ϕ} slice of relaxation time data hypercube $\tau(r, k)$ is an independent sample of the entire system dynamics, in that it shares the same statistical distribution with the whole dataset. Further analysis of $\tau(k_r)$ and TTCF calculation show that this technique can be useful in investigating structure-dynamic relationships and time-dependent dynamic processes such as aging.

Acknowledgements

This work was entirely supported by the Wisconsin Materials Research Science and Engineering Center. Primary experiments and data analysis were supported by DMR-1720415. Final analysis and manuscript preparation were supported by DMR-2309000. The authors thank Jittisa Ketkaew and Jan Schroers of Yale University for provision of the metallic glass nanowire samples. The authors gratefully acknowledge the use of facilities and instrumentation supported by the Wisconsin Materials Research Science and Engineering Center (DMR-1720415 and DMR-2309000).

Data Availability

5D STEM raw data, relaxation time data, and the data plotted in the figure are available through the Materials Data Facility (DOI: 10.18126/Y2VI-NTSK).

References

- [1] L. He, P. Zhang, M.F. Besser, M.J. Kramer, P.M. Voyles, Electron Correlation Microscopy: A New Technique for Studying Local Atom Dynamics Applied to a Supercooled Liquid, Microsc. Microanal. 21 (2015) 1026–1033. https://doi.org/10.1017/S1431927615000641.
- [2] P. Zhang, L. He, M.F. Besser, Z. Liu, J. Schroers, M.J. Kramer, P.M. Voyles, Applications and limitations of electron correlation microscopy to study relaxation dynamics in supercooled liquids, Ultramicroscopy. 178 (2017) 125–130. https://doi.org/10.1016/j.ultramic.2016.09.001.
- [3] P. Zhang, J.J. Maldonis, Z. Liu, J. Schroers, P.M. Voyles, Spatially heterogeneous dynamics in a metallic glass forming liquid imaged by electron correlation microscopy, Nat. Commun. 9 (2018) 1–7. https://doi.org/10.1038/s41467-018-03604-2.
- [4] D. Chatterjee, A. Annamareddy, J. Ketkaew, J. Schroers, D. Morgan, P.M. Voyles, Fast Surface Dynamics on a Metallic Glass Nanowire, ACS Nano. 15 (2021) 11309–11316. https://doi.org/10.1021/acsnano.1c00500.

- [5] K. Spangenberg, S. Hilke, G. Wilde, M. Peterlechner, Direct View on Non-Equilibrium Heterogeneous Dynamics in Glassy Nanorods, Adv. Funct. Mater. 31 (2021) 2103742. https://doi.org/https://doi.org/10.1002/adfm.202103742.
- [6] K. Nakazawa, K. Mitsuishi, Development of temporal series 4D-STEM and application to relaxation time measurement, Microscopy. 10 (2023) 1–4. https://doi.org/10.1093/jmicro/dfad006.
- [7] M.D. Ediger, S Patially H Eterogeneous D Ynamics in S Upercooled L Iquids, Annu. Rev. Phys. Chem. 51 (2000) 99–128. https://doi.org/10.1146/annurev.physchem.51.1.99.
- [8] R. Richert, Heterogeneous dynamics in liquids: fluctuations in space and time, J. Phys. Condens. Matter. 14 (2002) R703. https://doi.org/10.1088/0953-8984/14/23/201.
- [9] L. Berthier, G. Biroli, J.-P. Bouchaud, L. Cipelletti, W. van Saarloos, eds., Dynamical Heterogeneities in Glasses, Colloids, and Granular Media, Oxford University Press, 2011. https://doi.org/10.1093/acprof:oso/9780199691470.001.0001.
- [10] L. Berthier, G. Biroli, Theoretical perspective on the glass transition and amorphous materials, Rev. Mod. Phys. 83 (2011) 587–645. https://doi.org/10.1103/RevModPhys.83.587.
- [11] A. Coniglio, T. Abete, A. De Candia, E. Del Gado, A. Fierro, Dynamical heterogeneities: From glasses to gels, J. Phys. Condens. Matter. 20 (2008) 494239. https://doi.org/10.1088/0953-8984/20/49/494239.
- [12] C.P. Royall, S.R. Williams, The role of local structure in dynamical arrest, Phys. Rep. 560 (2015) 1–75. https://doi.org/https://doi.org/10.1016/j.physrep.2014.11.004.
- [13] S.M. Bhattacharyya, B. Bagchi, P.G. Wolynes, Subquadratic wavenumber dependence of the structural relaxation of supercooled liquid in the crossover regime, J. Chem. Phys. 132 (2010) 104503. https://doi.org/10.1063/1.3330911.
- [14] P.H. Handle, L. Rovigatti, F. Sciortino, Q-Independent Slow Dynamics in Atomic and Molecular Systems, Phys. Rev. Lett. 122 (2019) 175501. https://doi.org/10.1103/PhysRevLett.122.175501.
- [15] B. Ruta, S. Hechler, N. Neuber, D. Orsi, L. Cristofolini, O. Gross, B. Bochtler, M. Frey, A. Kuball, S.S. Riegler, M. Stolpe, Z. Evenson, C. Gutt, F. Westermeier, R. Busch, I. Gallino, Wave-Vector Dependence of the Dynamics in Supercooled Metallic Liquids, Phys. Rev. Lett. 125 (2020) 55701. https://doi.org/10.1103/PhysRevLett.125.055701.
- [16] B. Ruta, G. Baldi, Y. Chushkin, B. Rufflé, L. Cristofolini, A. Fontana, M. Zanatta, F. Nazzani, Revealing the fast atomic motion of network glasses, Nat. Commun. 5 (2014) 3939. https://doi.org/10.1038/ncomms4939.
- [17] N. Neuber, O. Gross, M. Frey, B. Bochtler, A. Kuball, S. Hechler, F. Yang, E. Pineda, F. Westermeier, M. Sprung, F. Schäfer, I. Gallino, R. Busch, B. Ruta, Disentangling structural and kinetic components of the α-relaxation in supercooled metallic liquids, Commun. Phys. 5 (2022) 316. https://doi.org/10.1038/s42005-022-01099-4.
- [18] G. Kumar, H.X. Tang, J. Schroers, Nanomoulding with amorphous metals, Nature. 457 (2009) 868–872. https://doi.org/10.1038/nature07718.
- [19] S. Huang, C. Francis, J. Sunderland, V. Jambur, I. Szlufarska, P.M. Voyles, Large Area, High Resolution Mapping of Approximate Rotational Symmetries in a Pd77.5Cu6Si16.5 Metallic Glass Thin Film, Ultramicroscopy. 241 (2022) 113612. https://doi.org/https://doi.org/10.1016/j.ultramic.2022.113612.

- [20] F. Yi, P. Tiemeijer, P.M. Voyles, Flexible formation of coherent probes on an aberration-corrected STEM with three condensers, Microscopy. 59 (2010) S15–S21. https://doi.org/10.1093/jmicro/dfq052.
- [21] D. Chatterjee, J. Wei, A. kvit, B. Bammes, B. Levin, R. Bilhorn, P. Voyles, An Ultrafast Direct Electron Camera for 4D STEM, Microsc. Microanal. 27 (2021) 1004–1006. https://doi.org/DOI: 10.1017/S1431927621003809.
- [22] C. Zhang, J. Feng, L.R. DaCosta, P.M. Voyles, Atomic resolution convergent beam electron diffraction analysis using convolutional neural networks, Ultramicroscopy. 210 (2020) 112921. https://doi.org/10.1016/j.ultramic.2019.112921.
- [23] S.H. Chung, J.R. Stevens, Time-dependent correlation and the evaluation of the stretched exponential or Kohlrausch–Williams–Watts function, Am. J. Phys. 59 (1991) 1024–1030. https://doi.org/10.1119/1.16640.
- [24] O.G. Shpyrko, X-ray photon correlation spectroscopy, J. Synchrotron Radiat. 21 (2014) 1057–1064. https://doi.org/10.1107/S1600577514018232.
- [25] S. Huang, P.M. Voyles, 5D-STEM of Real- and Reciprocal-space Resolved Dynamics in a Metallic Liquid, Microsc. Microanal. 29 (2023) 272–273. https://doi.org/10.1093/micmic/ozad067.124.
- [26] F.W.& H.W.Å. Francisco de la Peña, Eric Prestat, Vidar Tonaas Fauske, Pierre Burdet, Jonas Lähnemann, Petras Jokubauskas, Tom Furnival, Magnus Nord, Tomas Ostasevicius, Katherine E. MacArthur, Duncan N. Johnstone, Mike Sarahan, Joshua Taillon, Thomas Aarholt, pquinn-d, hyperspy/hyperspy: Release v1.7.3, (2022). https://doi.org/10.5281/zenodo.7263263.
- [27] R.T. Duncan Johnstone, Phillip Crout, Magnus Nord, Carter Francis, Joonatan Laulainen, Simon Høgås, Eirik Opheim, Ben Martineau, Tina Bergh, Eric Prestat, Niels Cautaerts, Stef Smeets, Håkon Wiik Ånes, Andrew Ross, Joseph Broussard, Sean Collins, Tom Furnival, pyxem/pyxem: pyxem 0.15.1, (2023). https://doi.org/10.5281/zenodo.7927374.
- [28] K. Paeng, H. Park, D.T. Hoang, L.J. Kaufman, Ideal probe single-molecule experiments reveal the intrinsic dynamic heterogeneity of a supercooled liquid, Proc. Natl. Acad. Sci. 112 (2015) 4952 LP 4957. https://doi.org/10.1073/pnas.1424636112.
- [29] P. Falus, L.B. Lurio, S.G.J. Mochrie, Optimizing the signal-to-noise ratio for X-ray photon correlation spectroscopy, J. Synchrotron Radiat. 13 (2006) 253–259. https://doi.org/10.1107/S0909049506006789.
- [30] K. Paeng, L.J. Kaufman, Single molecule rotational probing of supercooled liquids, Chem. Soc. Rev. 43 (2014) 977–989. https://doi.org/10.1039/c3cs60186b.
- [31] A. Arbe, J. Colmenero, Characterization of the "simple-liquid" state in a polymeric system: Coherent and incoherent scattering functions, Phys. Rev. E Stat. Nonlinear, Soft Matter Phys. 80 (2009) 1–13. https://doi.org/10.1103/PhysRevE.80.041805.
- [32] K. Nakazawa, K. Mitsuishi, I. Konstantin, S. Kohara, K. Tsuchiya, Structure-Dynamics Correlation in Metallic Glass Revealed by 5-Dimensional Scanning Transmission Electron Microscopy, arXiv (2023). https://doi.org/10.48550/arXiv.2305.06521.
- [33] V.N. Novikov, K.S. Schweizer, A.P. Sokolov, Coherent neutron scattering and collective dynamics on mesoscale, J. Chem. Phys. 138 (2013) 164508. https://doi.org/10.1063/1.4802771.
- [34] M. Aichele, J. Baschnagel, Glassy dynamics of simulated polymer melts: Coherent scattering and

- van Hove correlation functions Part II: Dynamics in the α -relaxation regime, Eur. Phys. J. E. 5 (2001) 245–256. https://doi.org/10.1007/s101890170079.
- [35] S. Karmakar, C. Dasgupta, S. Sastry, Growing length scales and their relation to timescales in glass-forming liquids, Annu. Rev. Condens. Matter Phys. 5 (2014) 255–284. https://doi.org/10.1146/annurev-conmatphys-031113-133848.
- [36] S. Whitelam, L. Berthier, J.P. Garrahan, Dynamic criticality in glass-forming liquids, Phys. Rev. Lett. 92 (2004) 1–4. https://doi.org/10.1103/PhysRevLett.92.185705.
- [37] S. Karmakar, C. Dasgupta, S. Sastry, Growing length and time scales in glass-forming liquids, Proc. Natl. Acad. Sci. U. S. A. 106 (2009) 3675–3679. https://doi.org/10.1073/pnas.0811082106.
- [38] E. Flenner, G. Szamel, Dynamic heterogeneity in a glass forming fluid: Susceptibility, structure factor, and correlation length, Phys. Rev. Lett. 105 (2010) 1–4. https://doi.org/10.1103/PhysRevLett.105.217801.
- [39] V.M. Giordano, B. Ruta, Unveiling the structural arrangements responsible for the atomic dynamics in metallic glasses during physical aging, Nat. Commun. 7 (2016) 10344. https://doi.org/10.1038/ncomms10344.
- [40] I. Gallino, D. Cangialosi, Z. Evenson, L. Schmitt, S. Hechler, M. Stolpe, B. Ruta, Hierarchical aging pathways and reversible fragile-to-strong transition upon annealing of a metallic glass former, Acta Mater. 144 (2018) 400–410. https://doi.org/10.1016/j.actamat.2017.10.060.
- [41] A. Das, P.M. Derlet, C. Liu, E.M. Dufresne, R. Maaß, Stress breaks universal aging behavior in a metallic glass, Nat. Commun. 10 (2019) 5006. https://doi.org/10.1038/s41467-019-12892-1.
- [42] A. Madsen, A. Fluerasu, B. Ruta, Structural Dynamics of Materials Probed by X-Ray Photon Correlation Spectroscopy BT Synchrotron Light Sources and Free-Electron Lasers: Accelerator Physics, Instrumentation and Science Applications, in: E. Jaeschke, S. Khan, J.R. Schneider, J.B. Hastings (Eds.), Springer International Publishing, Cham, 2018: pp. 1–30. https://doi.org/10.1007/978-3-319-04507-8 29-2.
- [43] Z. Evenson, B. Ruta, S. Hechler, M. Stolpe, E. Pineda, I. Gallino, R. Busch, X-ray photon correlation spectroscopy reveals intermittent aging dynamics in a metallic glass, Phys. Rev. Lett. 115 (2015) 1–5. https://doi.org/10.1103/PhysRevLett.115.175701.